RSC Advances

PAPER

View Article Online
View Journal | View Issue

Cite this: *RSC Adv.*, 2022, **12**, 6791

Template-free preparation of iron oxide loaded hollow silica spheres and their anticancer proliferation capabilities

Sultan Akhtar, *[a] Seyda Tugba Gunday,[a] Amany I. Alqosaibi, [b] Hanan Aldossary,[c] Ayhan Bozkurt *[a] and Firdos Alam Khan [d]

Received 9th November 2021
Accepted 15th February 2022

DOI: 10.1039/d1ra08216g

rsc.li/rsc-advances

Hollow silica spheres (HSS) exhibited high-specific surface area, low toxicity, low density, and good biocompatibility. The effectivity of HSS material can be improved further by loading nanoparticles for smart biological applications. In this work, magnetic nanoparticle (iron oxide; Fe_3O_4)-loaded pure HSS (c-HSS-Fe) were synthesized successfully using a template-free chemical route and investigated for their anticancer cell proliferation capabilities against cancerous cell lines: human colorectal carcinoma cells (HCT-116). The structure, morphology, chemical bonding, and thermal stability of the prepared HSS derivatives were studied using spectroscopic and microscopic techniques. Our analyses confirmed the successful preparation of Fe_3O_4 loaded HSS material (sphere diameter ~515 nm). The elemental analysis revealed the existence of Fe along with Si and O in the Fe_3O_4 loaded HSS material, thus reaffirming the production of the c-HSS-Fe product. The effects of silica spheres on HCT-116 cells were examined microscopically and by MTT assays. It was observed that the c-HSS-Fe demonstrated dose-dependent behavior and significantly reduced the cancer cell proliferation at higher doses. Our results showed that c-HSS-Fe was more effective and profound in reducing the cancer cells' activities as compared to unloaded HSS material where the cancer cells have undergone nuclear disintegration and fragmentation. It is concluded that c-HSS-Fe is a powerful bio-active material against cancerous cells.

1. Introduction

Silica nanoparticles exhibit various applications, *e.g.*, in the production of catalyst carriers, lithium batteries, ceramic industry, and gas sensors as well as in the biomedical field.[1] One of the main attributes of silica nanoparticles is that they can enhance the mechanical capabilities of thin films and thus are most useful in anti-corrosion and superhydrophobic applications.[2–4] One of the striking features of silica nanoparticles is that they can be produced in hollow forms,[5,6] and utilized in drug delivery systems, encapsulation, medical diagnostics, dental materials,[7,8] and bimolecular-release systems.[9,10] Moreover, hollow silica is a hard material with high porosity and excellent absorption properties, which make it useful in drug delivery, immunotherapy, cancer imaging, and cancer treatments.[10–17] Furthermore, mesoporous silica particles (MSPs) are used in drug delivery applications due to their excellent properties, *e.g.* large surface area and pore volume, highly ordered channels, and size tuneable capabilities.[18–20] MMSN (magnetic nanoparticles loaded mesoporous silica nanospheres) displayed a pH-dependent drug release profile and a magnetically controlled drug release behavior.[21] In another study, multifunctional hollow mesoporous silica encapsulated with magnetic nanoparticles provides a promising platform for hyperthermia and chemotherapy for cancer treatment applications.[22] MMSNs with a raspberry-like rough surface synthesized *via* the oil-in-water emulsion method have shown great potential for drug loading and drug delivery into specific target cells, an advantage over conventional drug formulations.[23] Similarly, some other hollow structures, *e.g.*, hydroxyapatite microspheres displaying a hollow core and well-organized shell have shown extensive attraction in the field due to their low mass density, high surface area, cell proliferation, and drug loading capabilities including drug release and cell attachment features.[24]

Though mesoporous silica particles have shown potential biocompatible capabilities, the challenge is rising because of their dose-dependent toxic effects.[25] On the other hand, iron oxide magnetic nanoparticles (IONPs; Fe_3O_4)[26] are

[a]*Department of Biophysics Research, Institute for Research and Medical Consultations (IRMC), Imam Abdulrahman Bin Faisal University, P. O. Box 1982, Dammam 31441, Saudi Arabia. E-mail: suakhtar@iau.edu.sa; stgunday@iau.edu.sa; abozkurt@iau.edu.sa*

[b]*Department of Biology, College of Science, Imam Abdulrahman Bin Faisal University, P. O. Box 1982, Dammam 31441, Saudi Arabia. E-mail: amgosaibi@iau.edu.sa*

[c]*Department of Epidemic Disease Research, Institute for Research and Medical Consultations (IRMC), Imam Abdulrahman Bin Faisal University, P. O. Box 1982, Dammam 31441, Saudi Arabia. E-mail: haalhameem@iau.edu.sa*

[d]*Department of Stem Cell Research, Institute for Research and Medical Consultations (IRMC, Imam Abdulrahman Bin Faisal University, Post Box No. 1982, Dammam 31441, Saudi Arabia. E-mail: fakhan@iau.edu.sa*

advantageous because of their biocompatible properties[27] as well as their selective target and contrast enrichment properties in magnetic resonance imaging (MRI).[28] However, the IONPs products are lacked the consistent binding sites to bind the biomolecules on their surface during the drug delivery applications.[29] To overcome this problem, the mesoporous silica materials can be utilized for conducive drug delivery applications as they have a large interaction and pore volume for the coupling of biochemicals/biomolecules.[30] As an alternative, hollow silica spheres (HSS) have been produced chemically by using phenyl-tri-methoxy silane (PTMS). Despite various benefits, earlier prepared HSS was not very successful for cancer therapy applications because of their non-degradable phenyl groups,[6] a limiting factor for biological applications. To address this issue, recently, we have reported a facile chemical route consisting of two steps to synthesize the pure hollow silica spheres, without non-degradable phenyl groups using PTMS compound.[3] The newly synthesized silica spheres are prepared by hydrolysis of PTMS and making them useful for biomedical applications by removing their characteristics organic groups upon employing a controlled multi-calcination process. The prepared HSS product could serve the desired high surface area for the coupling or loading of magnetic nanoparticles into the silica spheres to enhance further their anticancer proliferation capabilities against cancerous cells.

In the present study, Fe_3O_4 loaded pure hollow silica spheres (c-HSS-Fe) are prepared successfully using a template-free synthetic route and tested for anticancer proliferation cells capabilities against human colorectal carcinoma (HCT-116) cells. After synthesis, the morphological and structural analyses of the prepared product are carried out using electron microscopy tools (scanning electron microscopy/energy dispersive X-rays spectroscopy (SEM/EDX), transmission electron microscopy/selected area electron diffraction (TEM/SAED)), X-rays diffraction (XRD), Fourier transform infrared spectroscopy (FTIR) and thermogravimetric analysis (TGA). The anticancer studies of the prepared: (1) uncalcined hollow silica spheres (u-HSS), (2) calcined hollow silica spheres (c-HSS), and (3) Fe_3O_4 loaded hollow silica spheres (c-HSS-Fe) are carried out against HCT-116 cells using morphometric and bioassay. The HCT-116 cells are experimentally treated with (1) u-HSS, (2) c-HSS, and (3) c-HSS-Fe products for 48 hours under four different concentrations (1, 3, 5, and 7 mg ml^{-1}). The important morphological features of the treated and untreated cells are examined by an inverted microscope and hence calculate the cell viability.

2. Materials and methods

2.1 Chemicals

Phenyltrimethoxysilane (PTMS) compound, ammonium hydroxide (NH_4OH), and nitric acid (HNO_3) (Sigma-Aldrich, Inc). Iron oxide (Fe_3O_4) nano-powder was supplied from US Research Nanomaterials, Inc. Milli-Q water purification system (Bedford, USA) was used to produce Ultrapure water. The synthesized products were labeled as, uncalcined hollow silica spheres (u-HSS), calcined hollow silica spheres (c-HSS), and iron oxide nanoparticles (Fe_3O_4) incorporated calcinated hollow silica spheres (c-HSS-Fe). A detailed description and synthesis reaction of the three products (u-HSS, c-HSS, and c-HSS-Fe) are given below. The 3-(4,5-dimethylthiazol-2-yl)-2,5-diphenyltetrazolium bromide (MTT) assay was used for measuring cell proliferation. De-ionized (DI) water was used for the preparation of HSS derivatives. The human colorectal carcinoma cells (HCT-116) used in this study were purchased from the American Type Culture Collection (ATCC), United States of America (USA).

2.2 Synthesis of u-HSS and c-HSS

First, the hollow silica spheres (HSS), uncalcined and calcined were synthesized according to our previously reported article.[3] A summary of the preparation of un-calcined HSS (u-HSS) and calcined HSS (c-HSS) products are given herein. By this method, u-HSS was synthesized by dissolving 0.96 ml PTMS in 80 ml of 6.6 mM HNO_3 solution and stirred in water media by placing it on a hot plate at a temperature of ~60 °C. The addition of 13.6 ml of NH_4OH (33%) solution into the PTMS triggered the condensation reaction, forming the uniform u-HSS. Correspondingly, the hydrolysis reaction progressed quickly within 3 minutes. The clear mixture rapidly transformed to a white color solution and precipitates were formed. The formed precipitates were washed with ethanol and then with DI-water after separating by centrifugation. The prepared particles were then dried at around 70 °C and labeled as u-HSS (uncalcined hollow silica spheres). The synthesized u-HSS, approximately 100 mg was taken and were kept in the furnace at a temperature of ~200 °C for 30 minutes. Subsequently, a calcination process was done on the same product at ~660 °C for 16 hours. The ramping rates for the first and second steps were set to be 5 and 1.5 °C $minute^{-1}$, respectively. The calcined product was labeled as c-HSS (calcined hollow silica spheres). The chemical process of c-HSS preparation is demonstrated as a schematic (see Fig. 1a). A digital photo of c-HSS powder is also shown.

2.3 Synthesis of Fe_3O_4 incorporated HSS (c-HSS-Fe)

For the preparation of magnetic nanoparticles (MNPs) loaded HSS (c-HSS-Fe), 60 mg of Fe_3O_4 powder and 50 ml of 6.6 mM HNO_3 solution were poured into 3-neck round bottom flask and shake for 10 minutes. Then, a volume of 0.6 ml of PTMS was put into the above-prepared solution and shaken altogether for 10 minutes. The obtained mixture was then placed into a water container at 60 °C and added 8.5 ml NH_4OH solution (33%). A milky solution was obtained upon adding the NH_4OH solution. This milky mixture was kept in a water bath for around 1 hour. The mixture was separated when the water bath was cooled down. Now, the collected mixture was stirred for almost 16 hours and applied centrifugation to remove the precipitated particles from the condensed solution at room temperature. Following this, the collected precipitates were washed initially with ethanol and then with DI water. After washing, the collected particles were calcinated first at around 250 °C for 3 hours and then at 660 °C for 8 hours and labeled the prepared product as c-HSS-Fe. The preparation reaction of c-HSS-Fe is

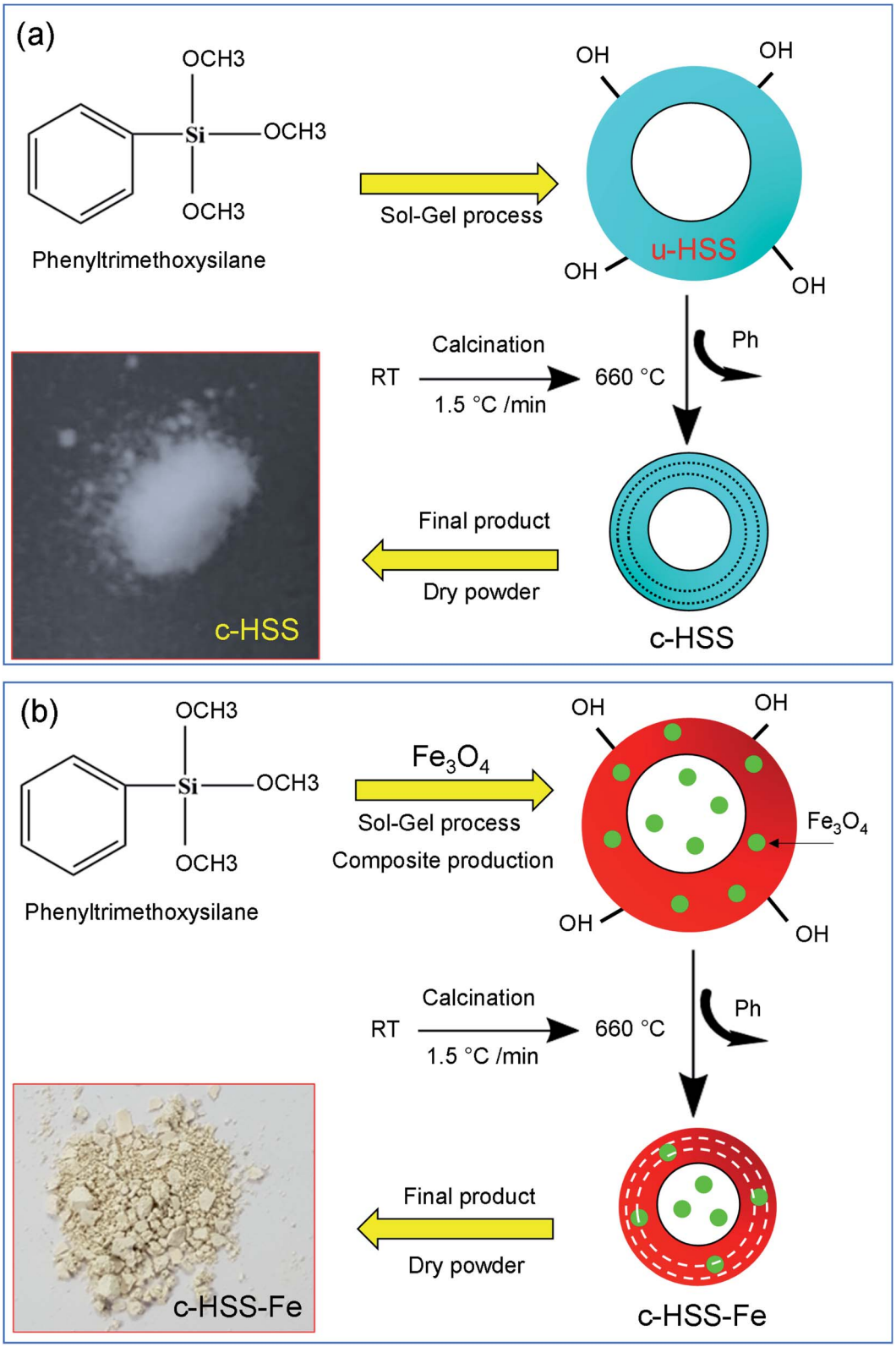

Fig. 1 The scheme of the preparation reaction of (a) u-HSS, c-HSS, and (b) Fe_3O_4 nanoparticles incorporated HSS (c-HSS-Fe). A photo of the final products (in powder form) is also shown. The powder of c-HSS-Fe is light brown while c-HSS is milky in color.

shown in Fig. 1b. The sample of c-HSS-Fe is turned to light brown from milky color after loading of Fe_3O_4 nanoparticles into silica spheres as observed for individual c-HSS samples.

2.4 Characterization (TEM, SEM, XRD, FTIR, and TGA)

Before their loading, the size and structure of the individual Fe_3O_4 nanoparticles were analyzed by transmission electron microscopy (TEM) (TEM Model: Morgagni 268, FEI, Czech Republic, operated at 80 keV). The morphological features and structural analysis of the prepared products, such as u-HSS, c-HSS, and Fe-HSS were also examined by TEM. For that purpose, a droplet of suspension of either u-HSS, c-HSS, or c-HSS-Fe was transferred onto a copper grid supported by a thin carbon layer to hold the specimen. The detail of the sample preparation is provided elsewhere.[31,32] From the TEM, the results for individual Fe_3O_4-NPs are plotted as size distribution in the size histogram. The crystalline features of the MNPs were verified by a selected area electron diffraction (SAED) pattern. Furthermore, the overall morphology of the u-HSS, c-HSS, and c-HSS-Fe products were evaluated by scanning electron microscopy (SEM) (Model SEM: Inspect S50, FEI, Czech Republic, operated at 20 kV). For elemental composition and elemental analysis, energy dispersive X-rays (EDX) spectroscopy was performed using an SEM instrument (TESCAN VEGA3 LM model, Czech Republic) equipped with an X-rays analyzer.

X-ray diffraction (XRD) of the c-HSS-Fe specimen was performed to confirm the existence of Fe_3O_4 in the silica spheres using XRD Diffractometer (Diffractometer Rigaku, Japan; copper-Kα radiations with wavelength = 0.154 nm). XRD instrument was operated at 40 kV and 15 mA. The FT-IR analyses (Fourier transform infrared spectroscopy, Shimadzu IR Spirit instrument) of u-HSS, c-HSS, and c-HSS-Fe were performed in the range of 400–4000 cm^{-1}. The thermal stability of u-HSS, c-HSS, and c-HSS-Fe was examined by Thermogravimetric analysis (TGA) (STA, PerkinElmer 6000, USA) between 25 to 700 °C.

2.5 Treatment of u-HSS, c-HSS, and c-HSS-Fe to cancer cells

The cytotoxic effect of u-HSS, c-HSS, and c-HSS-Fe was analyzed on human colorectal carcinoma cells (HCT-116).[33] The cells were purchased from the American Type Culture Collection (ATCC), United States of America (USA). The cancerous cells were grown in the cultured media using a CO_2 incubator (Thermo-scientific, Waltham, MA, USA) at a temperature of 37 °C.[34] Thereafter, the cells were treated with three prepared products: c-HSS, u-HSS, and c-HSS-Fe (0, 3, 5, and 7 mg ml^{-1}). Upon completing the treatments, the treated cancer cells were examined by using an inverted microscope to study the variations that happen in the morphology of the cells due to exposure to silica particles.

2.6 Cancer cells morphology and viability by MTT assay

MTT assay were carried out to examine the effect of three prepared products: c-HSS, u-HSS, and c-HSS-Fe on cancer cells (HCT-116). For this purpose, the grown cancer cells were exposed with as-prepared silica spheres (c-HSS, u-HSS, and c-HSS-Fe) under four different concentrations (1, 3, 5, and 7 mg ml^{-1}); each treatment for 48 hours. For the control group cells, c-HSS, u-HSS, and c-HSS-Fe were not added otherwise kept in the same experimental conditions as done for treated specimens. Then the cancerous cells were exposed with MTT (5 mg ml^{-1}) for 4 hours and then media was replaced with DMSO (dimethyl sulfoxide). The optical density (OD) of the samples was measured plate reader at 570 nm wavelength. Finally, the cell viability (in %) of each specimen was found out by the following relation:

$$\text{Cell viability (in \%)} = \left[\frac{\text{OD}_{\text{(c-HSS, u-HSS \& c-HSS-Fe-treated cells)}}}{\text{OD}_{\text{(control cells)}}}\right] \times 100$$

The samples were processed for OD reading by utilizing the ELISA plate reader, where light has 570 nm wavelength. The control and the treated specimens with different doses were visualized under an inverted light microscope. The digital photographs of the specimens were recorded at a representative magnification of 400× to highlight the important morphological features of each specimen. In addition, the statistical analysis for the control and the treated cells (u-HSS to HCT-116, c-HSS to HCT-116, and c-HSS-Fe to HCT-116) was performed by applying the GraphPad Software.

3. Results and discussion

3.1 Morphological and structural analysis

SEM and TEM are commonly used to analyze the surface morphology and structure of the nanomaterials at high resolution. Fig. 2 shows the morphological analysis of the Fe_3O_4 particles and the three-silica products; u-HSS, c-HSS, and c-HSS-Fe. It was observed that the nano-powder of Fe_3O_4 exhibited spherical-shaped particles with a bit of agglomeration (Fig. 2a). Several particles, more than 250 individual particles were selected from different TEM images and their size was measured. The results of this measurement were drawn in the form of a size histogram (Fig. 2b). The average diameter of the particles was found 14.2 ± 1.4 nm. Nearly the same sized Fe_3O_4 nanoparticles were incorporated into mesoporous hollow silica nanocapsules prepared by either sol–gel route or emulsion polymerization.[21–23] The Fe_3O_4 nanoparticles showed the polycrystalline nature when analyzed by electron diffraction as judged by the appearance of several rings in the SAED pattern (Fig. 2c). The first 5-rings of the SAED pattern started from the inner ring are indexed as, (220), (311), (400), (511), and (440), confirming the structure of the Fe_3O_4 crystal.[35,36] Fig. 2d–f shows the SEM micrographs of u-HSS, c-HSS, and c-HSS-Fe (Fe_3O_4 doped HSS) specimens. As per TEM analysis, the silica spheres appeared monodispersed and showed a well-organized and uniform spherical texture. The size of u-HSS was measured from the SEM micrographs, which were found to be around 760 nm (Fig. 2d).[5,6] Upon applying the calcination step, the size of c-HSS was reduced substantially because of the removal of phenol groups from the HSS (Fig. 2e). This observation was verified when the average diameter of the c-HSS

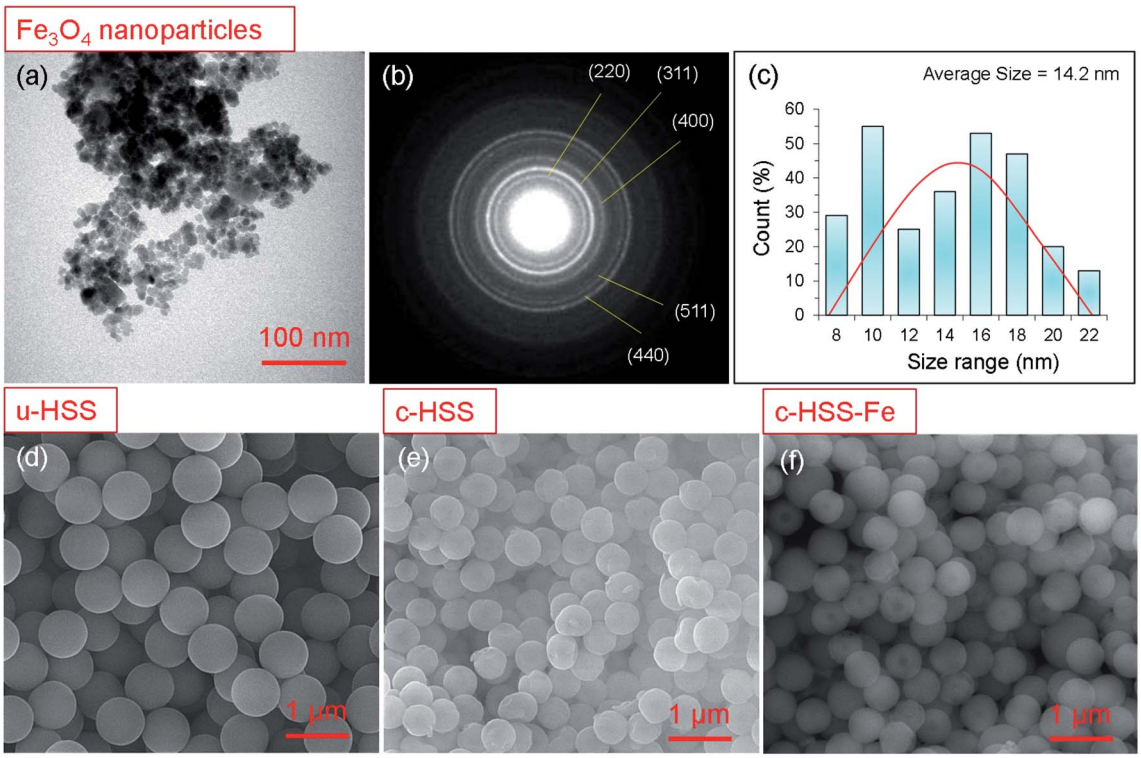

Fig. 2 Morphology and size analysis of the Fe_3O_4 nanoparticles and hollow silica spheres (HSS). (a) TEM image, (b) SAED pattern, and (c) size histogram of Fe_3O_4 particles. The average diameter of the particles is ~14 nm. (c) SAED pattern of the Fe_3O_4 nanoparticles, showing the polycrystalline nature, the first 5-rings of the pattern are indexed as, (220), (311), (400), (511), and (440). SEM micrographs of (d) u-HSS, (e) c-HSS and (f) c-HSS-Fe. The scale bars are: 100 nm (a), 1 μm (d–f).

specimen was estimated which was found to be 515 ± 15 nm. Nearly, a similar size and morphology were found for the magnetic nanoparticles incorporated silica specimen (c-HSS-Fe), suggesting no further modifications or changes were happening in the morphology of the spheres concerning size and shape after loading of Fe particles (see Fig. 2f).

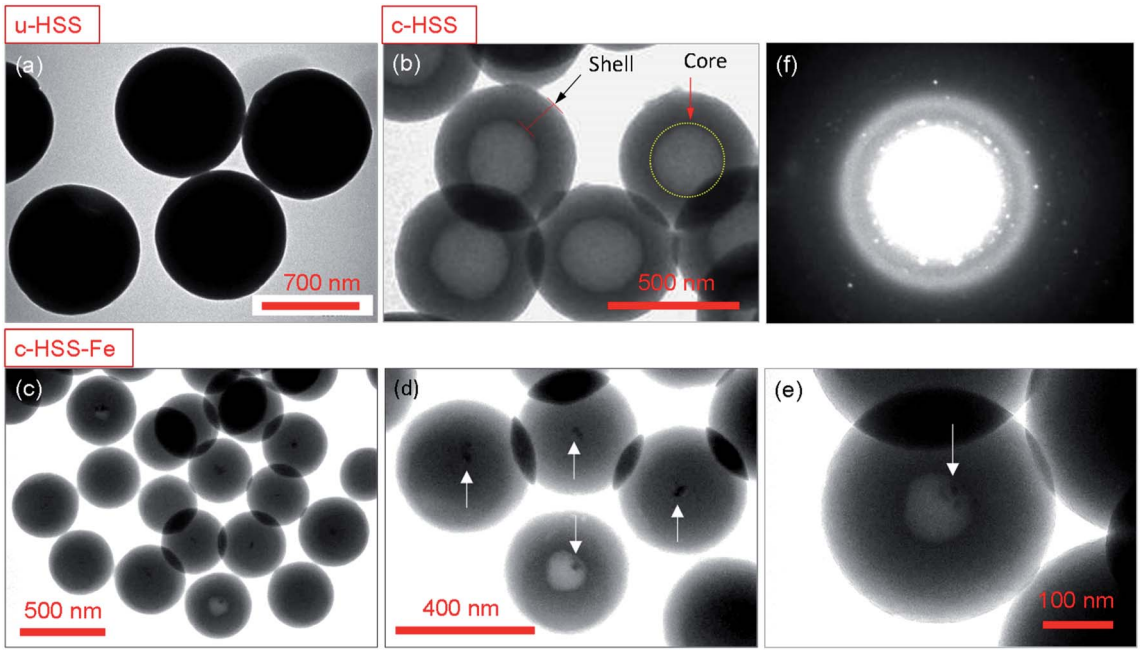

Fig. 3 Morphology, size, and structural analyses of the hollow silica spheres (HSS). TEM image of (a) uncalcined HSS, (b) calcined HSS, and (c–e) c-HSS-Fe specimen at three different magnifications. The Fe_3O_4 nanoparticles are highlighted by arrows. (f) SAED pattern of the c-HSS-Fe specimen showing the dots of the Fe_3O_4 nanoparticles. The scale bars are: 700 nm (a), 500 nm (b and c), 400 nm (d) and 100 nm (e).

All prepared products, u-HSS, c-HSS, and c-HSS-Fe were further analyzed by TEM, particularly to confirm further the loading of Fe_3O_4 nanoparticles into the HSS (Fig. 3). Fig. 3a displayed the morphology of several uncalcined spheres (u-HSS specimen), where several uncalcined silica spheres are shown. As analyzed by TEM, the u-HSS were larger in diameter compared to c-HSS and c-HSS-Fe specimens (see Fig. 3a–c). This was expected due to the presence of phenyl groups attached to silica that produced larger HSS. This result is consistent with the observation made earlier by SEM (Fig. 3). Furthermore, the TEM images resolved the obvious hollow structure of the spheres as evident by the bright contrast in the middle of the spheres, especially visible in the calcinated specimens. The shells of the spheres were appeared darker compared to hollow cores due to their solid nature by scattering more electrons than the thin/hollow cores. The shell/core structure was more evident for the c-HSS specimen (Fig. 3b), where the brightness of the image was increased a bit to clarify the core and shell structures. TEM micrographs showed clear evidence of the core structure of the silica spheres appearing with bright contrast as compared to the shell. The shell thickness of one sphere is marked with a black arrow and the core of the other sphere is highlighted with a yellow dotted circle and indicated by a red arrow. Fig. 3c–e showed the TEM micrographs of the c-HSS-Fe specimen at three different magnifications to highlight the obvious morphology of the silica spheres and to reveal the presence or loading of iron nanoparticles inside the spheres. Excitingly, the Fe_3O_4 nanoparticles that are coupled at the edges of the cores, are visible, the hollow nature of the core helps to reveal the ~14 nm-sized iron nanoparticles inside the cores under TEM. Few such Fe_3O_4 nanoparticles inside the core were highlighted by white arrows in Fig. 3d and e, identified by their darker contract

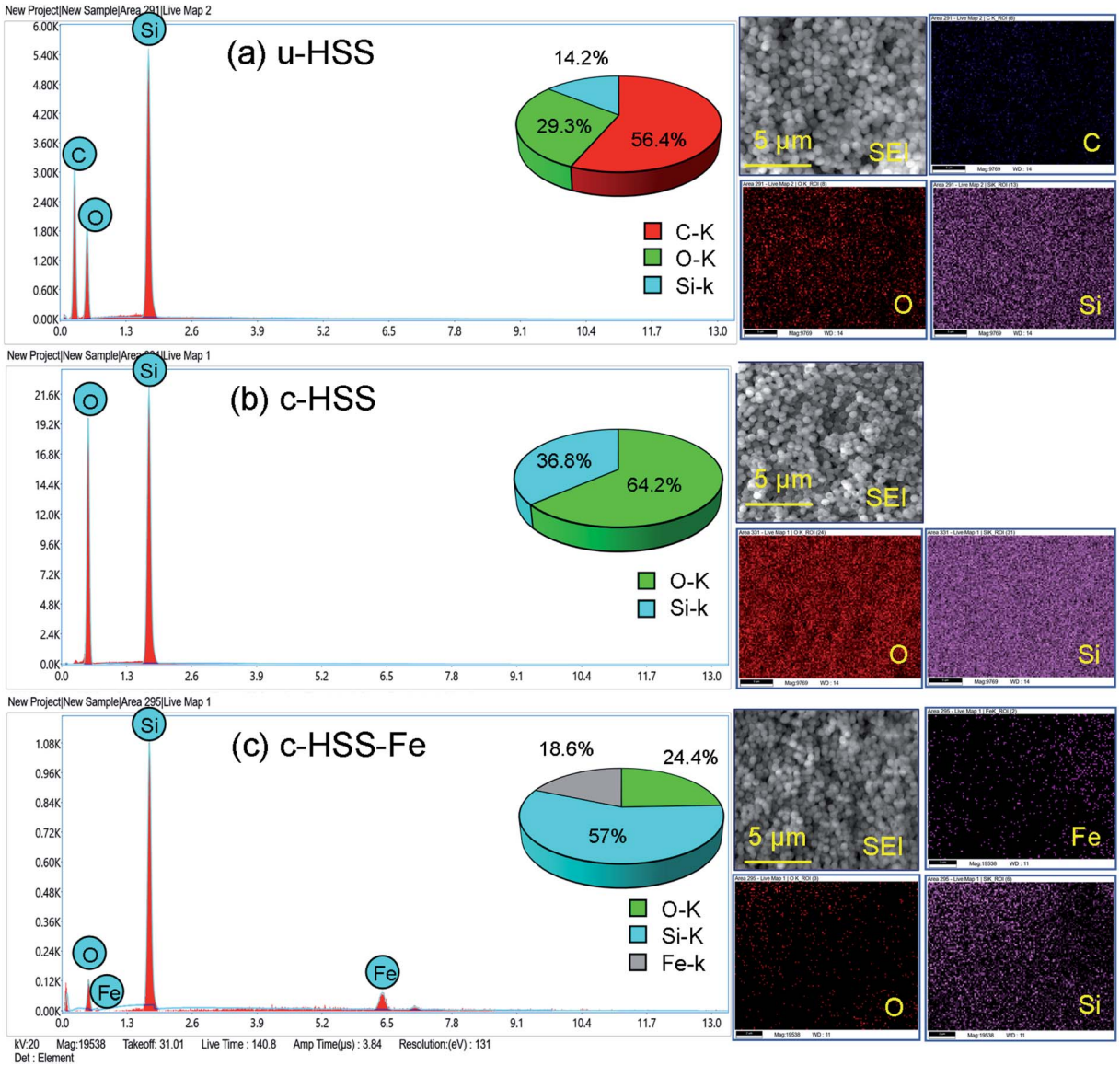

Fig. 4 Energy-dispersive X-ray spectroscopy (EDS) along with EDX elemental mapping of (a), u-HSS, (b) c-HSS, and (c) c-HSS-Fe. The concentration of constituent elements is shown inside of each spectrum in the form of a pi-graph.

compared to the hollow core. Due to their nature, the higher atomic number than Si, Fe_3O_4 scattered more electrons than hollow Si-core under TEM and generated darker contrast compared to Si-cores. Further to highlight the presence of the Fe_3O_4 nanoparticles, SAED was performed in the TEM for u-HSS and c-HSS and c-HSS-Fe specimens. Only the SAED pattern of the c-HSS-Fe displayed the dots in the pattern due to the co-existence of Fe_3O_4 nanoparticles (Fig. 4f), while the other two HSS specimens exhibited only blurred rings which are the signature of amorphous nature and the non-existence of any particles.[3] In summary, SEM, TEM and SAED analyses confirm the hollow structure and the successful loading of Fe_3O_4 nanoparticles into the hollow silica spheres.

The presence of Fe_3O_4 in the HSS product was further signified by performing EDS in the SEM. The results of EDX (EDX spectra along with elemental mapping) of u-HSS, c-HSS, and c-HSS-Fe specimens are presented in Fig. 4. SEM images from where each EDX spectrum was taken are also shown along with elemental mapping images. The EDX spectrum of u-HSS displayed the existence of carbon (C), oxygen (O), and silicon (Si) with a weight percentage of 56.4, 29.3, and 14.2, respectively. The presence of C content in the u-HSS specimen arrived from phenyl groups (Fig. 4a). The EDX spectrum and elemental mapping of the u-HSS displayed the distribution of C, O, Si, and lack of iron (Fe). The EDX spectrum of the c-HSS confirmed the removal of the organic groups from the HSS upon calcination as no peak was observed for C (Fig. 4b). The weight percentage of O and Si was obtained as follows: 64.2 (O) and 36.8 (Si). The EDX spectrum of the c-HSS-Fe specimen confirmed the presence of Fe in the HSS as the peak of the Fe can be seen at ~6.5 eV in the spectrum (Fig. 4c). The Fe peak was missing in both the spectra of u-HSS and c-HSS specimens. Furthermore, no peak was observed for C, verifying the absence of phenyl groups in the iron-loaded HSS (c-HSS-Fe specimen). The weight percentage of the three constituent elements is found as follows: 24.4 (O), 57 (Si), and 18.6 (Fe). The distribution of Fe along with O and Si was shown by EDX mapping, suggesting the uniform distribution of the Fe into the silica spheres. Thus, EDX analysis confirmed the presence of iron in the final HSS product (c-HSS-Fe specimen).

3.2 Structural analyses and a physical test

3.2.1 XRD analysis. Further to SEM and TEM, the XRD analysis was carried out on the c-HSS-Fe specimen to confirm the presence of Fe_3O_4 NPs in the silica spheres. Fig. 5a shows the results of the XRD powder pattern of c-HSS-Fe within the 2θ range of 15–70°. The broad diffraction peak at 20° (2θ degrees) marked with (*) symbol on the left shoulder is ascribed to the

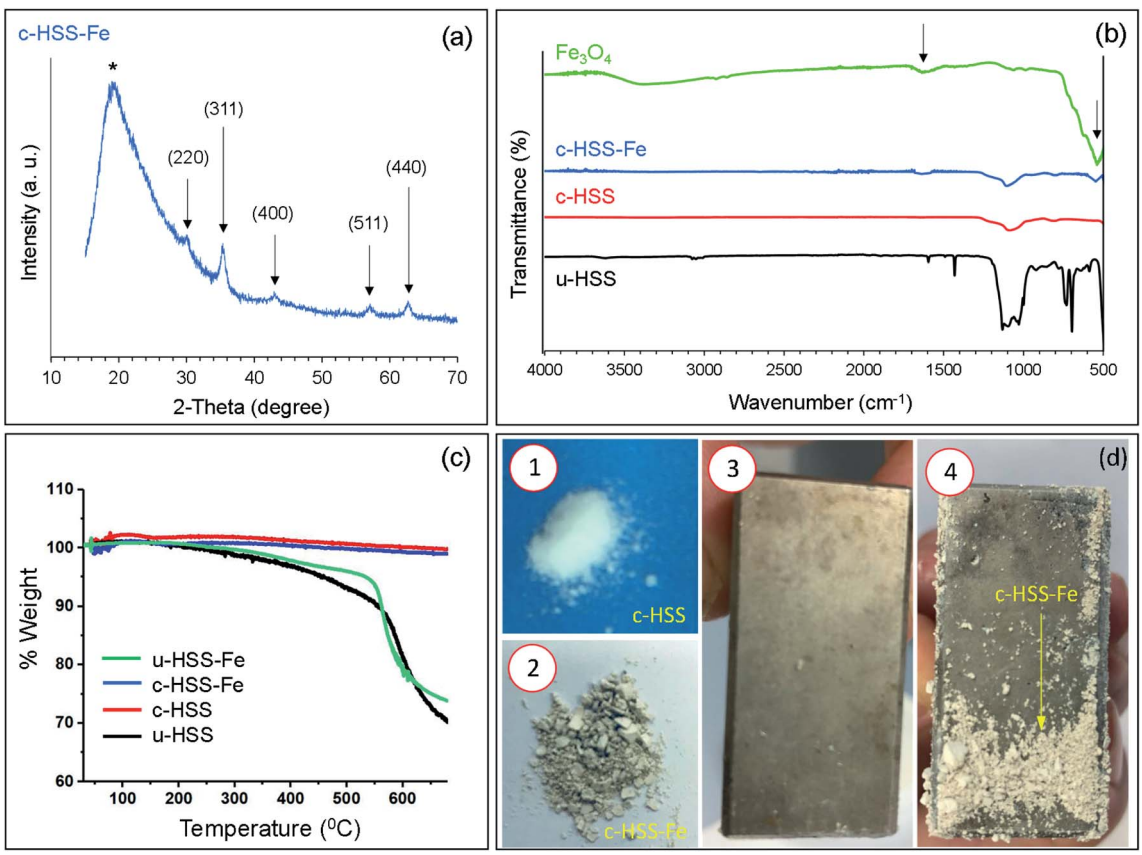

Fig. 5 (a) XRD pattern of the c-HSS-Fe. (b) FTIR spectra of the u-HSS, c-HSS, and c-HSS-Fe specimens. For comparison, FTIR spectra of individual Fe_3O_4 nanoparticles are also shown. (c) TG plots of the u-HSS, c-HSS, c-HSS-Fe, and u-HSS-Fe. (d) A digital photograph of the physical appearance of c-HSS (1) and c-HSS-Fe (2); the magnetic slab used to attract the c-HSS-Fe powder (3). The c-HSS-Fe powder can be seen attached to the magnetic slab after the test (4).

amorphous silica. The XRD patterns of u-HSS showed that silica spheres show a similar pattern.[3] The diffraction peaks of [2 2 0], [3 1 1], [4 0 0], [4 4 0], and [5 1 1] proved the existence of Fe_3O_4 spinel structure in the HSS, confirming the presence of magnetic nanoparticles within the silica spheres.[36] This result agrees with electron diffraction data shown earlier in Fig. 2c, where Fe_3O_4 nanoparticles were analyzed by the SAED pattern obtained by TEM. The intense peak/ring in both cases is (311).

3.2.2 FTIR analysis. FTIR analysis was conducted to explain the major chemical bonds of the individual silica spheres and Fe_3O_4 intercalated products (u-HSS, c-HSS c-HSS-Fe, and Fe_3O_4 nanoparticles) (Fig. 5b). Fig. 5b shows comparative FTIR spectra (started from bottom) of u-HSS (black), c-HSS (red), c-HSS-Fe_3O_4 (blue), and individual Fe_3O_4 nanoparticles (green). It can be seen that HSS shows a strong broad absorption band, belonging to Si–O–Si asymmetric stretching is located at ~1135 cm^{-1} in each HSS spectra (black, red, and blue). The symmetric and asymmetric stretching vibrations of Si–O peaks are seen at ~730 and ~492 cm^{-1}, respectively. The absorption at 970 cm^{-1} belongs to the bending vibration of Si–O units and a characteristic weak stretching centered at ~3500 cm^{-1} are assigned to Si-(O–H) groups. The phenyl groups which are linked to HSS show ~3120 cm^{-1} due to asymmetrical stretching vibration of aromatic CH groups, only available in the uncalcined HSS (u-HSS). It is clear that the calcination process diminished the strong asymmetric stretching of Si–O–Si at ~1135 and a new weak peak appeared at 1080 cm^{-1} (Fig. 5b). The weak absorptions at ~798 and ~445 cm^{-1} were assigned for Si–O symmetric stretching vibration. It is clear that all the peaks related to phenyl substances are detached and the c-HSS materials had only a pure silica matrix. The intercalation of Fe_3O_4 into HSS was confirmed by the distinctive peak stretching vibration associated with the metal–oxygen absorption (Fe–O bonds) at ~580 cm^{-1} (c-HSS-Fe, Fig. 5b).[37]

3.2.3 TGA analysis. TGA (thermo-gravimetric) plots of u-HSS, c-HSS, u-HSS-Fe, and c-HSS-Fe are shown in Fig. 5c. TGA plots of all the HSS specimens were plotted between temperature (25 to 700 °C) and percent weight loss (vertical scale). For c-HSS (red plot), a small weight change or weight loss was observed for the entire TG range 25 to 700 °C. On the other hand, the u-HSS specimen (black curve) started its weight loss or degradation at a temperature around 250 °C and continuous at higher temperatures, which is corresponding to the burning of organic species present in the HSS in the form of phenyl groups. In addition to the removal of organic molecules, a significant weight loss was noticed for magnetic nanoparticles incorporated HSS (u-HSS-Fe) after 550 °C (see green plot). The weight decay was attributed to the removal of impurities and oxygen from Fe_3O_4 under an inert atmosphere. The loss of impurities resulted in transformation to weak ferromagnetic hematite.[38] Contrary to u-HSS and u-HSS-Fe, the c-HSS-Fe specimen shows no visible weight change and remains constant from 25 °C to 700 °C (see blue graph). The behavior of TGA plots ofc-HSS and c-HSS-Fe were nearly similar to each other, which is no weight loss, highlighting the strong thermal stability of the iron-loaded HSS product. The nature of each specimen and preparation is given earlier by a schematic Fig. 1. The results of TGA were further explained by TEM analysis (see Fig. 2), where we have found that the average size of the c-HSS specimen was reduced, about 30% reduction in the size of the spheres (sphere diameter 760 to 510 nm). This size reduction was happened because of the removal of phenyl groups from the spheres after the multi-step calcination process. The thermal stability of the calcined spheres (c-HSS and c-HSS-Fe) was reaffirmed by SEM and TEM inspection and analyses (see Fig. 2 and 3), the morphology of HSS was not altered or affected after the calcination and doping of iron oxide nanoparticles. Hence, the thermally stable Fe_3O_4 doped HSS (c-HSS-Fe) were obtained after removing the organic groups from the u-HSS.

3.2.4 A physical test of c-HSS-Fe. The physical appearance of two products, c-HSS (1) and c-HSS-Fe (2) is shown in Fig. 5d. The c-HSS specimen showed the white milky color whereas c-HSS-Fe powder gave the blackish appearance, indicating the presence of Fe_3O_4 NPs in the product. The existence of Fe_3O_4 NPs in the HSS material was also confirmed by performing a simple test as shown by panels 3 and 4 of Fig. 5d. The c-HSS-Fe powder was pulled by magnetic slab as highlighted by the yellow arrow, while the c-HSS specimen showed no attraction to slab. The c-HSS-Fe powder attached to the magnetic slab can be seen in Fig. 5d (4), confirming the presence of magnetic nanoparticles in the sample. To clarify the surface morphology of the magnetic slab, a digital photograph of the same slab before the test was also shown in Fig. 5d (3).

3.3 Effect of u-HSS, c-HSS, and c-HSS-Fe on cancer cell morphology

The effect of u-HSS, c-HSS, and c-HSS-Fe particles on the morphology of the cancerous cells under different doses (0, 1, 3, 5, and 7 mg ml^{-1}) are shown in Fig. 6. The treatment of u-HSS (1 mg ml^{-1}) showed a little impact on the cancer cells as compared to cells of the control group (Fig. 6; upper row). The treatment of cells with a dose of 3 mg ml^{-1} showed a moderate effect where nuclear condensation of cancer cells was observed (Fig. 6c). The dosages of 5 and 7 mg ml^{-1} showed some changes in the morphology of the cancer cell but not many cells' deaths were observed. The post 48 hours treatment of c-HSS (1 mg ml^{-1}) showed a moderate level of nucleus condensation of the cells (Fig. 6, middle row). The treatment of 3 mg ml^{-1} showed a strong nuclear condensation and cell membrane disruption was found. The 5 and 7 mg ml^{-1} doses caused the loss of a cell large population. The treatment of c-HSS-Fe (1 mg ml^{-1}) showed a strong nucleus condensation of the cancer cells (Fig. 6b-bottom row). We did not observe any morphological changes in the control cells. The 3 mg ml^{-1} c-HSS-Fe treatment showed further nucleus condensation, whereas the dosages of 5 and 7 mg ml^{-1} caused the loss of the cancer cell population.

This is the first study where iron oxide nanoparticles are loaded to hollow silica spheres and tested their anticancer capabilities against human cancer cells (HCT-116). For example, multi-shelled dendritic mesoporous organo-silica was used in cancer immunotherapy.[15] In another report, hollow mesoporous silica nanocarriers were used for *in vivo* cancer imaging and therapy.[14] In addition to this, ytterbium (Yb) doped

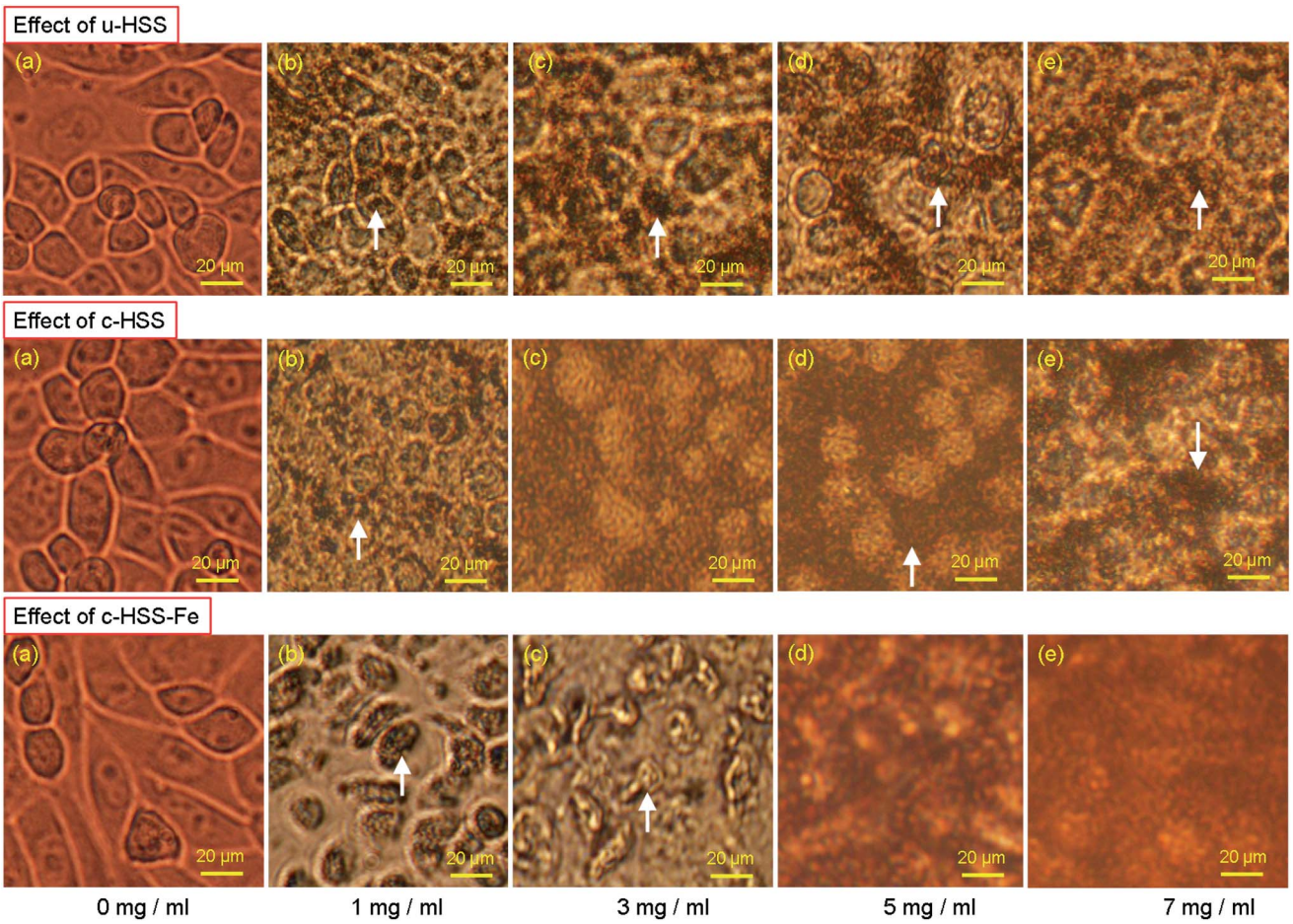

Fig. 6 Effect of u-HSS, c- and c-HSS-Fe on cancer cell morphology. Morphology of the cancer cells after treatment (48 h) with u-HSS (top row), c-HSS (middle row), and c-HSS-Fe (bottom row). (a) Control (0 mg ml^{-1}), (b) treated 1 mg ml^{-1}, (c) treated with 3 mg ml^{-1}, (d) treated with 5 mg ml^{-1} and (e) treated with 7 mg ml^{-1}. The arrows showed cellular disintegration, augmentation, and condensation. The scale bars are 20 µm.

yttrium oxide (Y_2O_3) nanoparticles (Y_2O_3–Yb) and double-shelled hollow spheres (Er@mSiO_2-Cu(x)S) have been used to enhance the chemo or photothermal anti-cancer therapy and dual-modal imaging.[39] Several studies have shown that azoles and their derivatives possess anti-cancer properties.[11,40–45] Furthermore, HCT-116 cells have been broadly tested as anti-cancer molecules anticancer drugs.[34,46–51]

3.4 Effect of u-HSS, c-HSS, and c-HSS-Fe on cancer cells survivability

The inhibition rate and the cell survivability (cell viability) of the HCT-116 cell line were examined by using MTT assay, the results are displayed in Fig. 7. The treatment of u-HSS specimen (dose concentration: 1, 3, 5, and 7 mg ml^{-1}) showed respectively, 85%,

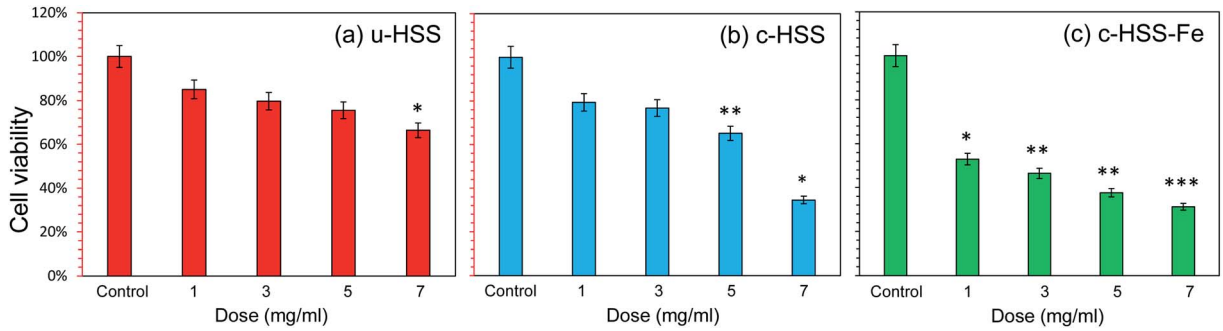

Fig. 7 Cancer cell viability by MTT assay: the HCT-cells were treated with u-HSS-c-HSS and c-HSS-Fe at different concentrations (0 mg ml^{-1}, 1 mg ml^{-1}, 3 mg ml^{-1}, 5 mg ml^{-1}, and 7 mg ml^{-1}) for 48 h. Data are the means ± SD of three different experiments. Difference between two treatment groups were analysed by student's test where (*p < 0.05; **p < 0.01; ***p < 0.001), p-values were calculated by student's test. No changes were observed for control specimens.

79%, 75%, and 66% cancer cell viability, whereas the treatment of c-HSS at same doses showed 79%, 76%, 65%, and 34% cell viability, respectively. When cancer cells were exposed to c-HSS-Fe spheres under four different concentrations (1, 3, 5, and 7 mg ml^{-1}), the cancer cell viability was significantly reduced to 53%, 46%, 37%, and 31%, respectively. From the cell viability assay, it was observed that u-HSS, c-HSS, and c-HSS-Fe have cytotoxic effects on the cancer cells. The results have been compared with already reported studies and reports. Similar results were reported earlier in the study where cancer cells were treated with hollow silica showed enhanced chemo and photothermal anti-cancer activity.[39] In another study, it has been reported that multi-shelled mesoporous silica nanospheres showed better optical cancer imaging.[52] In another study, hollow microspheres and doxorubicin (DOX) were employed to induce anti-cancer activity.[53] It was reported that silica nanoparticles can be biocompatible with dependence on size, concentration, and other parameters.[53] M. R. Dzamukova *et al.* have shown that the pronounced toxic effect of magnetic particles on mammalian cells and organisms was absent and did not induce apoptosis in either cancer cells or primary cells.[27,54–56]

4. Conclusion

In this study, pure hollow silica spheres (c-HSS) and iron oxide (Fe_3O_4) loaded hollow silica spheres (c-HSS-Fe) were synthesized successfully using a simple two-step method which is followed by multi-step calcination. After characterization, the prepared materials were tested for anti-cancer aptitudes on human colorectal carcinoma cells (HCT-116). The morphology and the loading of Fe_3O_4 nanoparticles into HSS were confirmed by electron microscopy and spectroscopic techniques. It was observed that the average size of the silica spheres was reduced significantly upon calcination with the fact that the accompanied phenol groups are removed after heating. Importantly, the HSS products displayed the monodispersed morphology with an average sphere size slightly above 700 nm (uncalcined HSS) and ~500 nm for calcined and Fe_3O_4 loaded HSS. EDX analysis further highlights the existence of Fe along with Si and O in the doped HSS, thus verifying the loading of Fe_3O_4 into c-HSS. Anticancer cells proliferation capabilities of the three prepared products, u-HSS, c-HSS and c-HSS-Fe were investigated against HCT-116 cells by using laser microscopy and MTT assays. It was found that the iron-loaded HSS reduced the cancer cells proliferation significantly and demonstrate a dose-relevant behavior. The smaller dose, 1 mg ml^{-1} produced a minor effect, whereas the higher doses (3, 5, and 7 mg ml^{-1}) reduced the cancer cell proliferation substantially. Furthermore, the doped and undoped HSS showed differential actions on cancer cells under the same conditions, c-HSS-Fe was the more effective and profound compound in terms of reducing the cancer cells proliferation. The results of this study showed that c-HSS-Fe could be a powerful bio-active material against cancerous cells.

Funding

The current work was supported by Deanship of scientific research (DSR), Imam Abdulrahman Bin Faisal University (IAU), Dammam, project number 2017-567-IRMC.

Conflicts of interest

The authors declared that they do not have any conflict of interest.

Acknowledgements

Mr Dionecio and Mr Edwardson are acknowledged for their assistance in the cell culture bioassay and TEM sample preparation work, respectively.

References

1 B. O. Uysal and F. Z. Tepehan, Controlling the growth of particle size and size distribution of silica nanoparticles by the thin film structure, *J. Sol-Gel Sci. Technol.*, 2012, **63**(1), 177–186.
2 M. Ramezani, M. R. Vaezi and A. Kazemzadeh, Preparation of silane-functionalized silica films via two-step dip coating sol-gel and evaluation of their superhydrophobic properties, *Appl. Surf. Sci.*, 2014, **317**, 147–153.
3 S. Akhtar, et al., A novel approach to produce monodisperse hollow pure silica spheres, *J. Saudi Chem. Soc.*, 2018, 477–485.
4 S. Akhtar, et al., Enhancement of anticorrosion property of 304 stainless steel using silane coatings, *Appl. Surf. Sci.*, 2018, **440**, 1286–1297.
5 J. Hu, et al., A facile and general fabrication method for organic silica hollow spheres and their excellent adsorption properties for heavy metal ions, *J. Mater. Chem. A*, 2014, **2**(46), 19771–19777.
6 H. J. Hah, et al., Simple preparation of monodisperse hollow silica particles without using templates, *Chem. Commun.*, 2003, (14), 1712–1713.
7 U. S. Yushau, L. Almofeez and A. Bozkurt, Aminotriazole functional silica incorporated BisGMA/TEGDMA resins as dental nanocomposites, *Polym. Polym. Compos.*, 2019, **27**(8), 488–495.
8 U. S. Yushau, L. Almofeez and A. Bozkurt, Novel Polymer Nanocomposites Comprising Triazole Functional Silica for Dental Application, *Silicon*, 2020, **12**(1), 109–116.
9 C. Adhikari, et al., Drug delivery system composed of mesoporous silica and hollow mesoporous silica nanospheres for chemotherapeutic drug delivery, *J. Drug Delivery Sci. Technol.*, 2018, **45**, 303–314.
10 C. Rosu, et al., Polypeptide-Coated Silica Particles Dispersed in Lyotropic Liquid Crystals of the Same Polypeptide, *J. Phys. Chem. B*, 2016, **120**(29), 7275–7288.
11 X.-Q. Wang, et al., Design, synthesis and biological evaluation of novel hybrid compounds of imidazole scaffold-based 2-benzylbenzofuran as potent anticancer agents, *Eur. J. Med. Chem.*, 2013, **62**, 111–121.
12 J. Y. Jang, et al., Folate decorated hollow spheres of microporous organic networks as drug delivery materials, *Chem. Commun.*, 2018, **54**(29), 3652–3655.
13 R. C. Lv, et al., Synthesis, luminescence, and anti-tumor properties of MgSiO3:Eu-DOX-DPP-RGD hollow microspheres, *Dalton Trans.*, 2015, **44**(42), 18585–18595.

14 S. Yang, et al., Hollow Mesoporous Silica Nanocarriers with Multifunctional Capping Agents for In Vivo Cancer Imaging and Therapy, *Small*, 2016, **12**(3), 360–370.
15 Y. N. Yang, et al., Multi-shelled Dendritic Mesoporous Organosilica Hollow Spheres: Roles of Composition and Architecture in Cancer Immunotherapy, *Angew. Chem., Int. Ed.*, 2017, **56**(29), 8446–8450.
16 S. Mohapatra, et al., Multifunctional mesoporous hollow silica nanocapsules for targeted co-delivery of cisplatin-pemetrexed and MR imaging, *Dalton Trans.*, 2014, **43**(42), 15841–15850.
17 Y. Chen, H. R. Chen and J. L. Shi, Construction of Homogenous/Heterogeneous Hollow Mesoporous Silica Nanostructures by Silica-Etching Chemistry: Principles, Synthesis, and Applications, *Acc. Chem. Res.*, 2014, **47**(1), 125–137.
18 M. Nejabat, et al., Fabrication of acetylated carboxymethylcellulose coated hollow mesoporous silica hybrid nanoparticles for nucleolin targeted delivery to colon adenocarcinoma, *Carbohydr. Polym.*, 2018, **197**, 157–166.
19 Y. Zhang, et al., A simple route to magnetically separable mesoporous silica with high surface area and large pore: A recyclable catalyst for aldol reaction, *Catal. Commun.*, 2015, **69**, 92–96.
20 O. Esim, *et al.*, Nanomaterials for Drug Delivery Systems, in *New Developments in Nanosensors for Pharmaceutical Analysis*, ed. S. A. Ozkan and A. Shah, Academic Press, 2019, ch. 9, pp. 273–301.
21 L.-L. Yu and H. Bi, Facile synthesis and magnetic property of iron oxide/MCM-41 mesoporous silica nanospheres for targeted drug delivery, *J. Appl. Phys.*, 2012, **111**(7), 07B514.
22 F. Lu, et al., Iron oxide-loaded hollow mesoporous silica nanocapsules for controlled drug release and hyperthermia, *Chem. Commun.*, 2013, **49**(97), 11436–11438.
23 M. Pérez-Garnes, et al., Cytostatic and Cytotoxic Effects of Hollow-Shell Mesoporous Silica Nanoparticles Containing Magnetic Iron Oxide, *Nanomaterials*, 2021, **11**(9), 2455.
24 C. R. Zhang, et al., Recent progress on biomedical applications of functionalized hollow hydroxyapatite microspheres, *Ceram. Int.*, 2021, **47**(10), 13552–13571.
25 Z. Xiong, et al., A facile method for the room-temperature synthesis of water-soluble magnetic Fe3O4 nanoparticles: Combination of in situ synthesis and decomposition of polymer hydrogel, *Mater. Chem. Phys.*, 2011, **130**(1–2), 72–78.
26 C. Garcia, et al., Mesoporous Aluminosilicate Materials with Superparamagnetic γ-Fe2O3 Particles Embedded in the Walls, *Angew. Chem., Int. Ed.*, 2003, **42**(13), 1526–1530.
27 M. R. Dzamukova, et al., Cell surface engineering with polyelectrolyte-stabilized magnetic nanoparticles: A facile approach for fabrication of artificial multicellular tissue-mimicking clusters, *Nano Res.*, 2015, **8**(8), 2515–2532.
28 H. X. Wu, et al., pH-responsive magnetic mesoporous silica nanospheres for magnetic resonance imaging and drug delivery, *React. Funct. Polym.*, 2012, **72**(5), 329–336.
29 C. Fernandez-Lopez, et al., Highly Controlled Silica Coating of PEG-Capped Metal Nanoparticles and Preparation of SERS-Encoded Particles, *Langmuir*, 2009, **25**(24), 13894–13899.
30 Y. Teng, et al., Magnetic iron oxide nanoparticle-hollow mesoporous silica Spheres:Fabrication and potential application in drug delivery, *Curr. Appl. Phys.*, 2020, **20**(2), 320–325.
31 U. Baig, et al., Facile synthesis, characterization and antibacterial activity of nanostructured palladium loaded silicon carbide, *Ceram. Int.*, 2018, **44**(14), 16908–16914.
32 M. M. Gad, et al., Effect of zirconium oxide nanoparticles addition on the optical and tensile properties of polymethyl methacrylate denture base material, *Int. J. Nanomed.*, 2018, **13**, 283–292.
33 F. Khan, et al., FMSP-Nanoparticles Induced Cell Death on Human Breast Adenocarcinoma Cell Line (MCF-7 Cells): Morphometric Analysis, *Biomolecules*, 2018, **8**(2), 32.
34 F. A. Khan, et al., Fluorescent magnetic submicronic polymer (FMSP) nanoparticles induce cell death in human colorectal carcinoma cells, *Artif. Cells, Nanomed., Biotechnol.*, 2018, **46**(suppl 3), S247–S253.
35 M. A. Almessiere, et al., Effect of Nd-Y co-substitution on structural, magnetic, optical and microwave properties of NiCuZn nanospinel ferrites, *J. Mater. Res. Technol.*, 2020, **9**(5), 11278–11290.
36 H. Tombuloglu, et al., Iron oxide nanoparticles translocate in pumpkin and alter the phloem sap metabolites related to oil metabolism, *Sci. Hortic.*, 2020, **265**, 109223.
37 T. K. O. Vuong, et al., Synthesis of high-magnetization and monodisperse Fe3O4 nanoparticles via thermal decomposition, *Mater. Chem. Phys.*, 2015, **163**, 537–544.
38 B. H. Ong, et al., Thermal stability of magnetite (Fe3O4) nanoparticles, *MRS Online Proc. Libr.*, 2009, **1118**(1), 309.
39 D. Yang, et al., Y2O3:Yb,Er@mSiO2–CuxS double-shelled hollow spheres for enhanced chemo-/photothermal anti-cancer therapy and dual-modal imaging, *Nanoscale*, 2015, **7**(28), 12180–12191.
40 R. Kaur, et al., Recent Developments on 1,2,4-Triazole Nucleus in Anticancer Compounds: A Review, *Anti-Cancer Agents Med. Chem.*, 2016, **16**(4), 465–489.
41 M. I. Soares, et al., Chiral 6,7-bis(hydroxymethyl)-1H,3H-pyrrolo[1,2-c]thiazoles with anti-breast cancer properties, *Eur. J. Med. Chem.*, 2013, **60**, 254–262.
42 R. N. Khaybullin, et al., Synthesis and anticancer evaluation of complex unsaturated isosteviol-derived triazole conjugates, *Future Med. Chem.*, 2015, **7**(18), 2419–2428.
43 V. Kumar, et al., Pyrazole containing natural products: Synthetic preview and biological significance, *Eur. J. Med. Chem.*, 2013, **69**, 735–753.
44 N. R. Jabir, et al., The Use of Azoles Containing Natural Products in Cancer Prevention and Treatment: An Overview, *Anti-Cancer Agents Med. Chem.*, 2018, **18**(1), 6–14.
45 Y. C. Duan, et al., Design and synthesis of novel 1,2,3-triazole-dithiocarbamate hybrids as potential anticancer agents, *Eur. J. Med. Chem.*, 2013, **62**, 11–19.
46 H. V. Sudeep, et al., Viwithan, a Standardized Withania somnifera Root Extract Induces Apoptosis in Murine

Melanoma Cells, *Pharmacogn. Mag.*, 2018, **13**(suppl 4), S801–S806.

47 C. Mazewski, K. Liang and E. G. de Mejia, Comparison of the effect of the chemical composition of anthocyanin-rich plant extracts on colon cancer cell proliferation and their potential mechanism of action using in vitro, in silico, and biochemical assays, *Food Chem.*, 2018, **242**, 378–388.

48 K. Matsuoka, et al., Effective Sequential Combined Chemotherapy with Trifluridine/Tipiracil and Regorafenib in Human Colorectal Cancer Cells, *Int. J. Mol. Sci.*, 2018, **19**(10).

49 Y. Liu, et al., N-Aryltriazole ribonucleosides with potent antiproliferative activity against drug-resistant pancreatic cancer, *Bioorg. Med. Chem. Lett.*, 2010, **20**(8), 2503–2507.

50 J. J. Li, *Top Drugs: History, Pharmacology, Syntheses*, Oxford University Press, 2015.

51 A. Sinha, et al., Induction of apoptosis in a human colorectal cancer cell line, HCT-116 by a vanadium- Schiff base complex, *Biomed. Pharmacother.*, 2017, **92**, 509–518.

52 C. C. Huang, W. Huang and C. S. Yeh, Shell-by-shell synthesis of multi-shelled mesoporous silica nanospheres for optical imaging and drug delivery, *Biomaterials*, 2011, **32**(2), 556–564.

53 R. Lv, et al., Synthesis, luminescence, and anti-tumor properties of MgSiO3:Eu-DOX-DPP-RGD hollow microspheres, *Dalton Trans.*, 2015, **44**(42), 18585–18595.

54 M. R. Dzamukova, et al., A Direct Technique for Magnetic Functionalization of Living Human Cells, *Langmuir*, 2011, **27**(23), 14386–14393.

55 E. A. Naumenko, et al., Nano-labelled cells—a functional tool in biomedical applications, *Curr. Opin. Pharmacol.*, 2014, **18**, 84–90.

56 H. Markides, M. Rotherham and A. J. El Haj, Biocompatibility and Toxicity of Magnetic Nanoparticles in Regenerative Medicine, *J. Nanomater.*, 2012, **2012**, 614094.